Supporting information

Scalable Fluorine-Free Superhydrophobic photo-thermal Coating Based on Boron Carbide and Candle Soot for Anti-Icing and photo-thermal De-Icing

Qingxi Li[1,2], Junshuo Pan[3], Haojie Wang[1], Tianchi Chen[*1,2], Xiangning Lu[*1].

1. School of Mechanical and Electrical Engineering, Jiangsu Normal University, Xuzhou 221000, China.

2. Sichuan Key Technology Engineering Research Center for All-electric Navigable Aircraft, Sichuan Guanghan, 618307, China

*Corresponding author：ctc900112@163.com, lxnam89@163.com

1.Testing details

1.1 Mechanical Durability and Chemical Stability Tests

1.1.1 Sandpaper Abrasion Test

Coated samples (20 mm × 20 mm) were placed horizontally on a flat platform. A 400# silicon carbide sandpaper (compliant with FEPA P400, particle size ~35 μm) was placed in contact with the coating surface. A 100 g weight (applying ~2.45 kPa pressure) was placed on top of the sample. A horizontal force was applied to move the sample at a constant speed of 5 cm/s, with a sliding distance of 20 cm per cycle. A total of 50 abrasion cycles were performed (total sliding distance: 10 m). After every 10 cycles, the WCA and SA were measured at room temperature using 5 μL deionized water droplets. All measurements were repeated 3 times (n = 3) to obtain average values with standard deviations.

1.1.2 Tape Peeling Test

The 25 mm × 25 mm sample was placed horizontally. 3M 600 transparent adhesive tape (width: 19 mm, adhesion strength: 3.5 N/cm) was fully applied to cover the coating surface. A 100 g weight was rolled back and forth on the tape to ensure uniform adhesion. The tape was then peeled off rapidly at 180° angle. This process was repeated for a total of 200 peeling cycles, with WCA and SA measured after every 20 cycles using 5 μL deionized water droplets. Each test was performed in triplicate (n = 3).

1.1.3 Sand Impact Test

The impact resistance was evaluated using a falling sand apparatus. 25 mm × 25 mm samples were mounted at 40° inclination. Quartz sand (100–200 mesh, particle size: 74–150 μm) was released freely from a container placed ~30 cm above the sample surface. The total sand mass ranged from 0 to 2000 g, applied in increments with 5 impact cycles per measurement point. WCA and SA were measured after every 5 cycles using 5 μL deionized water droplets. All tests were performed in triplicate (n = 3).

1.1.4 pH Tolerance Test

25 mm × 25 mm samples were placed horizontally. Aqueous solutions with pH values ranging from 1 to 14 were prepared (pH adjusted using HCl for acidic and NaOH for alkaline conditions). 50 μL droplets of each pH solution were placed on the coating surface and covered with watch glasses to prevent evaporation. After 1 h exposure at 23 ± 2 °C, droplets were removed by rinsing with deionized water, and WCA and SA were measured immediately. For immersion

testing, samples were immersed in deionized water, pH 1 HCl solution, pH 14 NaOH solution, and ethanol for 3 h, then rinsed, dried, and measured. Each pH condition was tested with 3 parallel samples (n = 3).

1.1.5 Long-term Acid/Alkali Immersion Test

Experimental Details: 25 mm × 25 mm samples were fully immersed vertically in:acidic solution: pH = 1 (adjusted with HCl), alkaline solution: pH = 14 (adjusted with NaOH). Immersion was conducted in sealed glass containers at room temperature (23 ± 2 °C). The liquid volume to sample area ratio was maintained at 10 mL/cm² (~6.25 mL per sample). WCA and SA were measured at regular intervals during 200 min (3.3 h) immersion. Before each measurement, samples were removed, rinsed with deionized water, and dried with nitrogen gas. All tests were repeated 3 times (n = 3).

1.1.6 Extreme Environment Stability Test

25 mm × 25 mm samples were subjected to: Extreme temperatures: −40 °C (cryogenic chamber) and 160 °C (convection oven), each for 12 h. UV aging: UVA-340 nm lamps at room temperature followed by total 12 h exposure. High humidity: 93 ± 3% RH at 25 ± 2 °C for 12 h. WCA and SA were measured every 2 h during exposure using 5 μL deionized water droplets. All tests were performed with 3 parallel samples (n = 3).

1.2 Experiments on Passive Anti-icing and De-icing

To investigate the passive anti-icing and active de-icing properties of the coating, experiments were carried out in an environmental test chamber (Model TL-100, China April Environmental Testing Equipment Co., Ltd.). The passive anti-icing performance was evaluated under conditions of temperatures ranging from –10 °C to –40 °C and 25% relative humidity. A camera was used to record the freezing process and measure the icing delay time of 20 μL water droplets placed on the coating surface. The icing delay time is defined as the duration from the liquid state until the droplet is completely frozen.

For the active de-icing tests, the coating was first subjected to temperatures from –10 °C to –30 °C. A xenon lamp simulating one-sun solar radiation were used to melt ice beads on the coating surface, and the melting time was recorded. Subsequently, under the same environmental conditions, the melting time of an ice layer (approximately 2 mm thick, formed by water freezing on the coating at –20 °C) .

1.3 Experiment on the Ice adhesion strength

The samples were placed in a environmental test chamber with the temperature and humidity set to -30°C and 35 ± 5% RH, respectively. A acrylic column with a base area of 100 mm^2 and a

height of 5 cm was placed on the samples, deionized water was injected into the column, and the deionized water was completely frozen after 1 hours. After the samples were completely fixed, the force transducer was mounted on the motion stage to push the column at a rate of 0.2mm/s. The maximum force was recorded to calculate the ice adhesion strength by the equation:

$$\tau_{ice} = \frac{F_{max}}{A} \quad \text{(S1)}$$

where A stands for the contact area between the ice and surface. ice adhesion strength were average values for 3 times.

2. Calculation details

S1. Calculating the light absorption efficiency

Light absorbance of the samples is calculated through the following equation:

$$A\% = 1 - R\% - T\% \quad \text{(S2)}$$

where A is the absorbance, R is the reflectance, and T is the transmittance.

S2. Calculating the photothermal conversion efficiency

The photothermal conversion efficiency of samples, η, which was defined as the ratio of the heat generated by the photothermal conversion of the surface to the input of solar power, and the calculation formula is as follows:

$$\eta = \frac{Q}{q \times A} \quad \text{(S3)}$$

where Q is the total heat generated by the surface, q represents the light intensity of sunlight (1kW/m^2), A is the surface area of the surface (6.25 cm^2).

When the surface temperature of samples and the surrounding temperature gradually reach a balance, the heat generated by the surface can be calculated as follows:

$$Q = h \times A \times (T_{sub} - T_{surr}) \quad \text{(S4)}$$

where h is the convective heat transfer coefficient of the substrate, A is the heat transfer area, T_{sub} is the equilibrium temperature of the surface, and T_{surr} is the temperature of surrounding temperature.

The convective heat transfer coefficient of the samples can be calculated by the following equation:

$$h = \frac{N\mathrm{u} \times \lambda}{L} \quad \text{(S5)}$$

where L is the characteristic length of heat transfer area (L=2.5), λ is the thermal conductivity of air, N_u is the Nusselt number, and can be calculated as follows:

$$N\mathrm{u} = 0.54 \times (Gr \times \mathrm{Pr})_m^{1/4} \quad \text{(S6)}$$

where $Gr = \frac{g a_v \Delta T L^3}{v^2}$ is the Grashof number, Pr is the prandtl number, the m represents qualitative temperature, which use arithmetic average temperature of the boundary layer ($T_m = \frac{T_{sub} + T_{surr}}{2}$). a_v is the expansion coefficient of air ($a_v = \frac{1}{T}$), T is the average of the sum of the initial ambient and equilibrium temperatures of the sample, g is the gravitational acceleration (9.8 m/s^2). ΔT is the value of the temperature difference in surface from room temperature to equilibrium temperature, ν is the viscosity coefficient.

S3. The heat-transfer model of a droplet on the different surfaces

The finite element simulation methods were performed by COMSOL, and the detailed method was explained as follows:

(1) The initial ambient temperature was -20 °C, the initial temperature of water droplet was 0 °C. We neglected the evaporation of water and sublimation of ice in the cooling conditions.

(2) The CA of the water droplet on the hydrophilic surface was 30°, the CA of the water droplet on the hydrophobic surface was 130°, the CA of the water droplet on the superhydrophobic surface was 150°.

(3) The classical heat and mass transfer equations were still feasible.

$$\frac{\partial(\rho C_p T)}{\partial t} + \nabla(\rho C_p u T) = \nabla[\nabla(kT)] \quad \text{(S7)}$$

(4) The networks near the heat transfer interfaces was set to hyperfine structure. The minimum interval step of time simulation was 0.001s.

S4. The Light absorption and heat-transfer mode

To better understand and further investigate the mechanisms of light absorption and photothermal conversion, a multiphysics model coupling electromagnetics and heat transfer was used, and COMSOL software was employed to simulate the surface multilevel structures. To obtain the electric field in the system, our COMSOL model solved the time-independent electromagnetic wave equation:

$$\nabla \times \nabla \times \boldsymbol{E}(\boldsymbol{r},\omega) - k_0^2 \varepsilon(\boldsymbol{r},\omega)\boldsymbol{E}(\boldsymbol{r},\omega) = 0 \quad \text{(S8)}$$

Where E is the electric field, k 0 is the free - space wavenumber, ε(r,ω) is the space - and wavelength - dependent relative permittivity of the material, and ω is the angular frequency of the incident light. The conversion of light energy to thermal energy can be expressed by Formula (S7).

$$\rho C_p \frac{\partial T}{\partial t} - \nabla \cdot (k \nabla T) = Q_r - Q_c \quad \text{(S9)}$$

Where T is the temperature, t is time; ρ,C_p and k are the density, specific heat capacity and thermal conductivity of the material under consideration, respectively. In addition, Q_r is the local thermal power of the TiN absorber. The generated thermal power Q_r can be obtained from Equation (S8).

$$Q_r = \frac{\omega \epsilon_0}{2} Im\{\varepsilon(\boldsymbol{r},\omega)\}|E(\boldsymbol{r},\omega)|^2 \quad \text{(S10)}$$

Where ε 0 is the vacuum permittivity, and Im{ε(r,ω)} is the imaginary part of the permittivity. Qc is the dissipated energy transferred from the absorber to the external environment, which can be expressed as

$$Q_c = B(T - T_{amb}) \quad \text{(S11)}$$

Where B is the heat transfer coefficient from the absorber to the external environment, and T amb is the ambient temperature (293.15 K).

3. Supplementary Figures

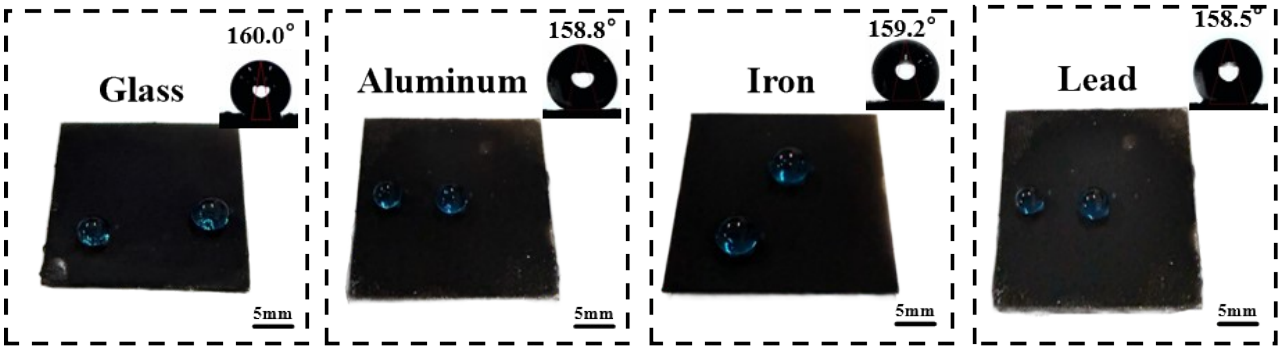

Fig. S1 Optical images of Candle@BC Coating on the different substrates.

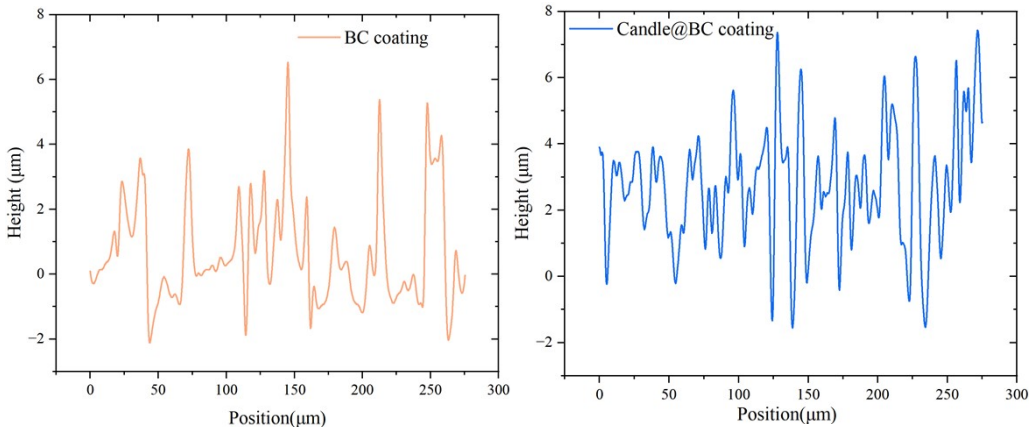

Fig. S2 Two-dimensional Surface Roughness of Candle@BC Coating.

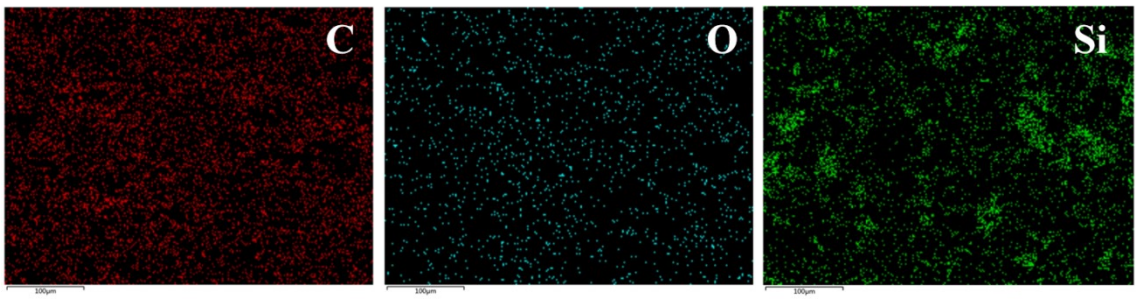

Fig. S3 EDS Spectrum of BC Coated Surface.

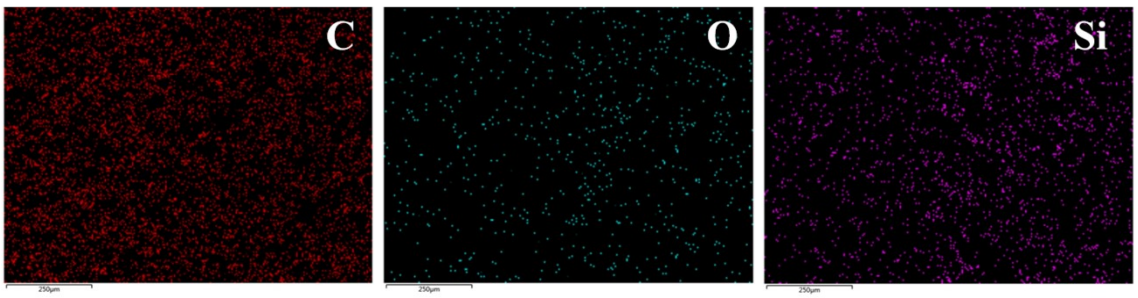

Fig. S4 EDS Spectrum of Candle@BC Coated Surface.

Fig. S5 Bouncing experiment of 50μL droplet on Candle@BC surface.

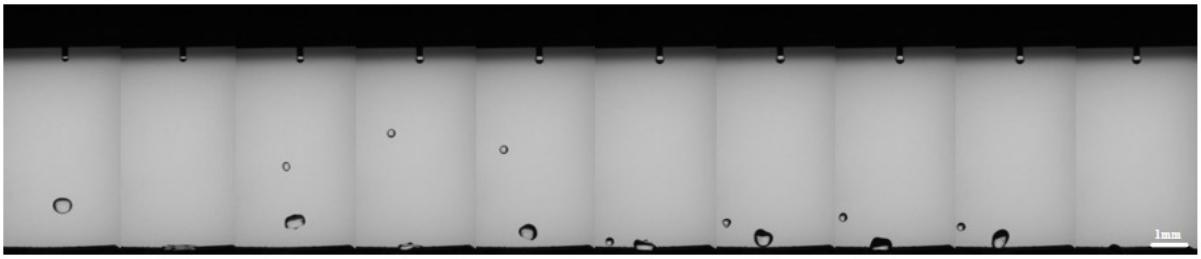

Fig. S6 Bouncing experiment of high liquid droplet on Candle@BC surface.

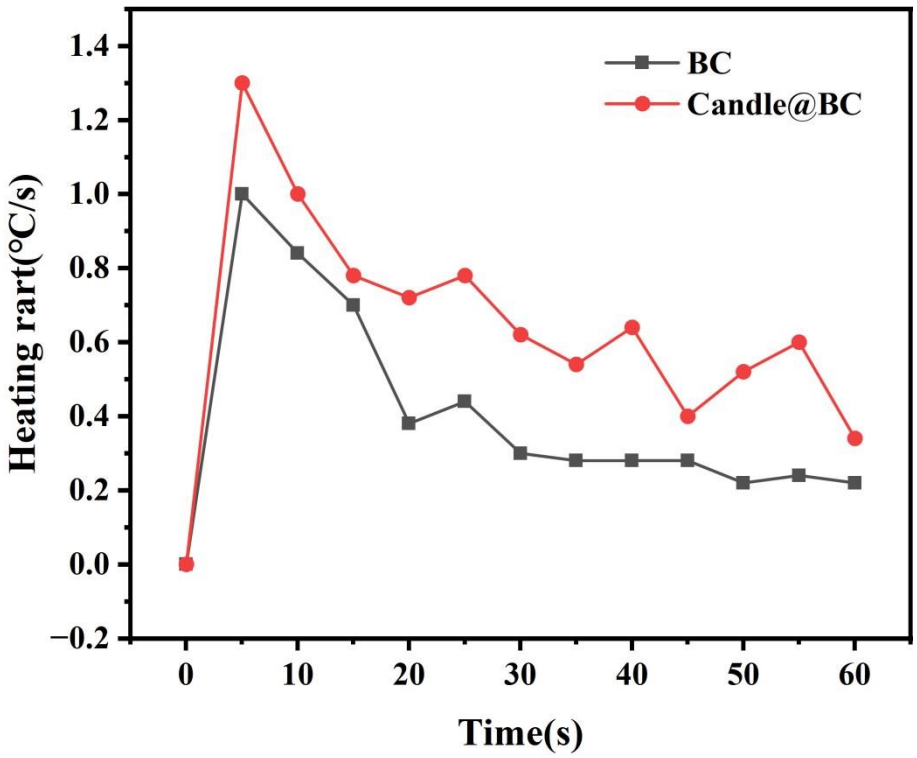

Fig. S7 Rate of temperature rising.

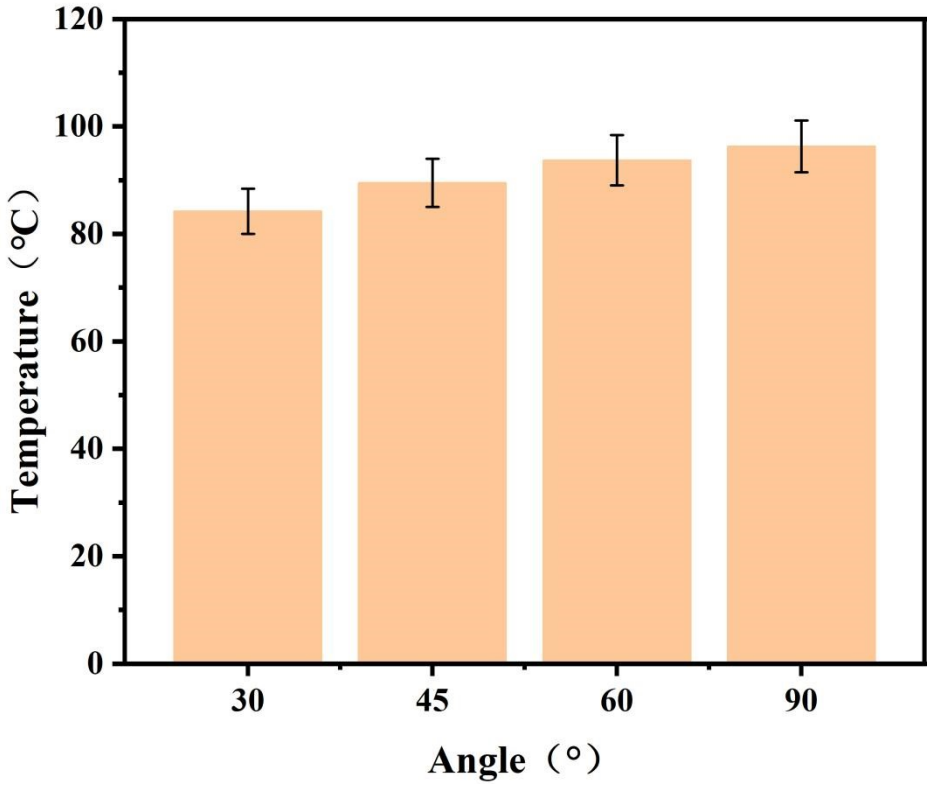

Fig. S8 Stable temperature of Candle@BC coating under different illumination angles.

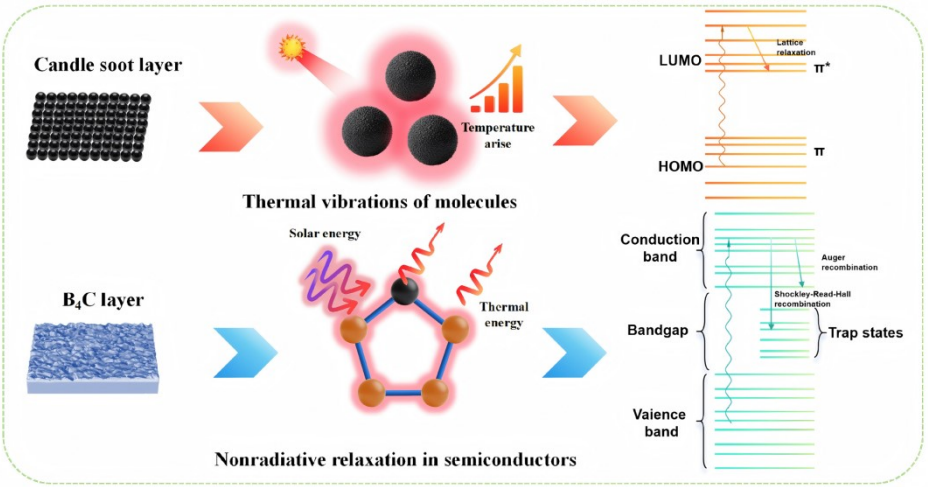

Fig. S9 Photothermal conversion mechanism

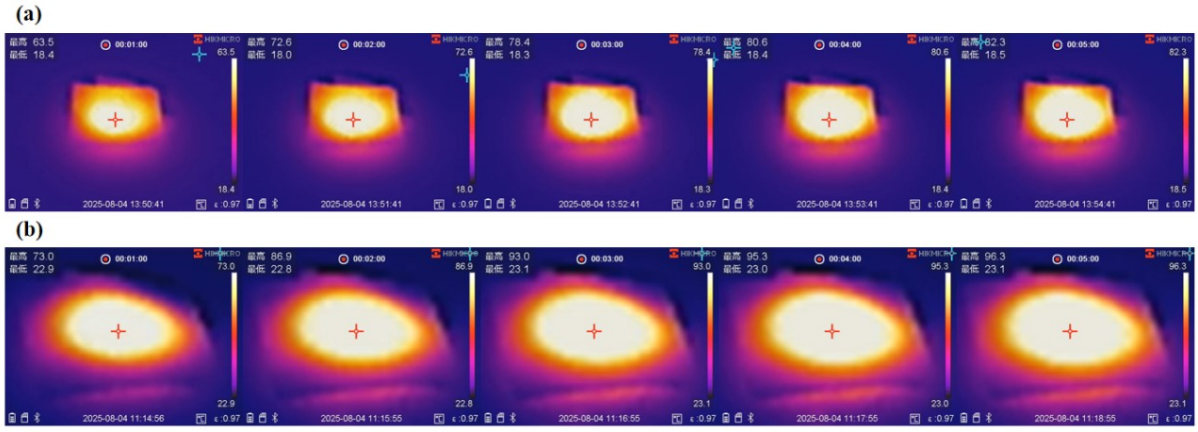

Fig. S10 (a) Thermal imaging image of temperature rise for BC coating (b) Thermal imaging image of temperature rise for Candle@BC coating.

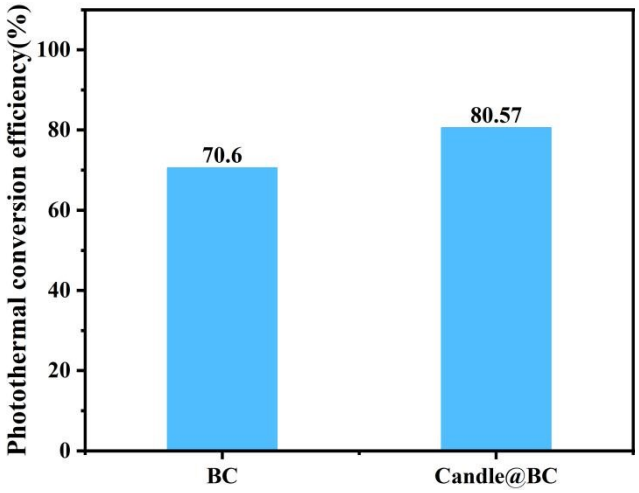

Fig. S11 Photothermal Conversion Efficiency of BC Coating and Candle@BC Coating.

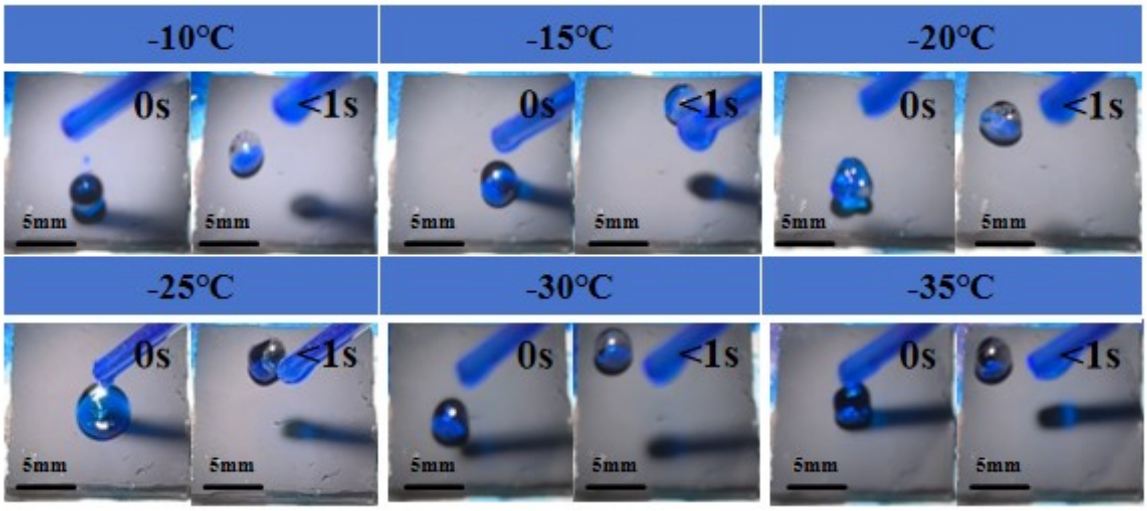

Fig. S12 Experimental Study on the Photothermal Anti-icing of Candle@BC Surface under Different Ambient Temperature.

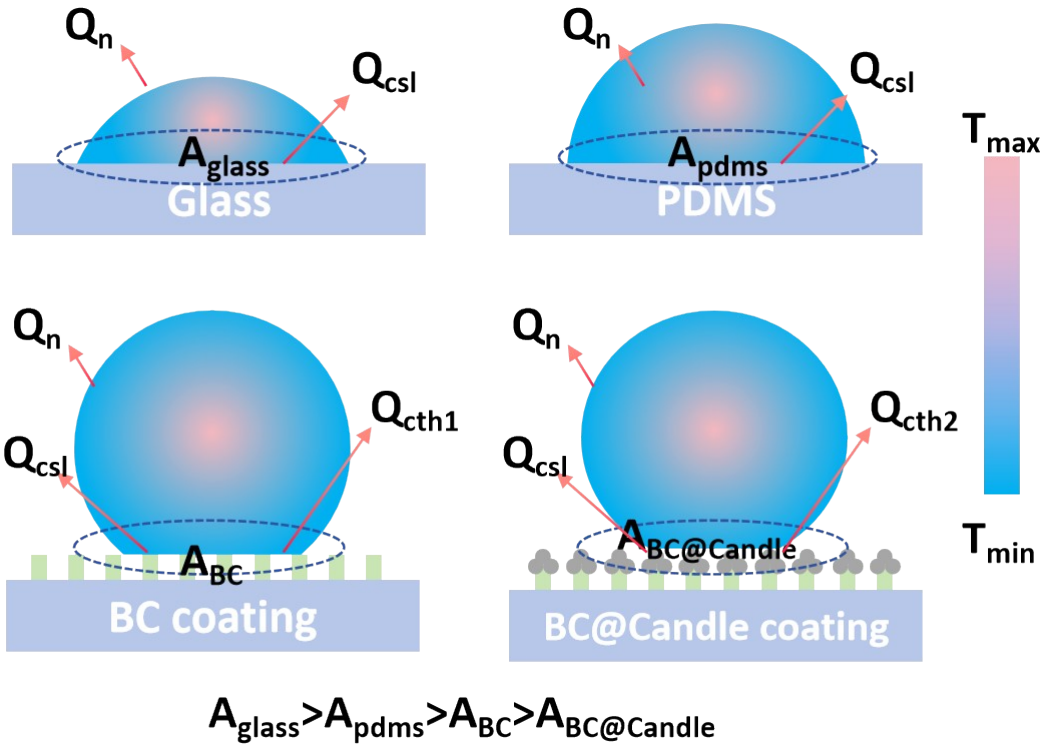

Fig. S13 Schematic of delayed icing heat exchange on the specimen surface

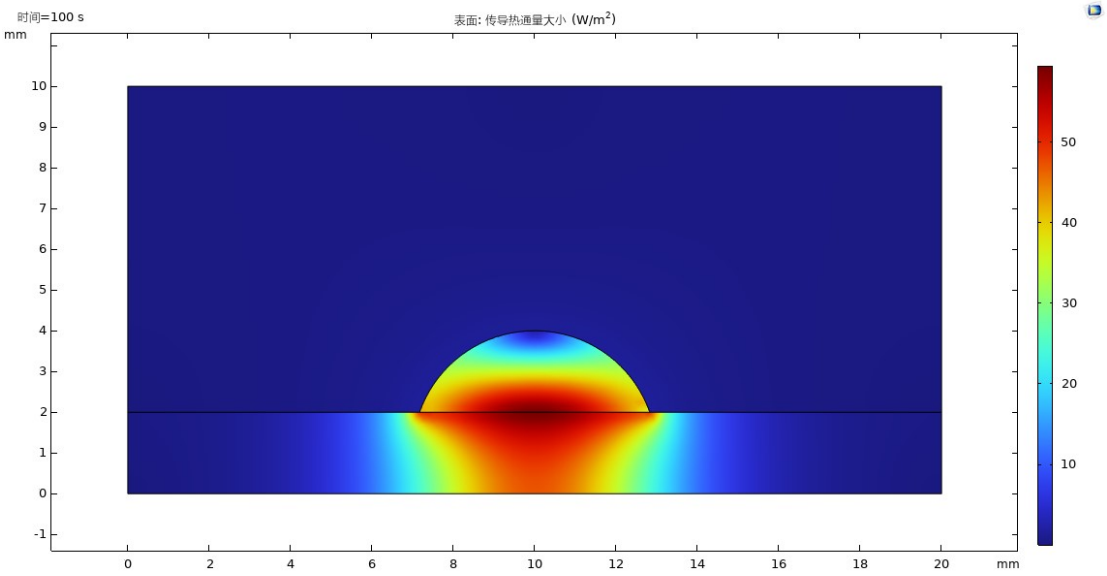

Fig. S14 The thermal conductivity behavior of glass surface simulated by COMSOL.

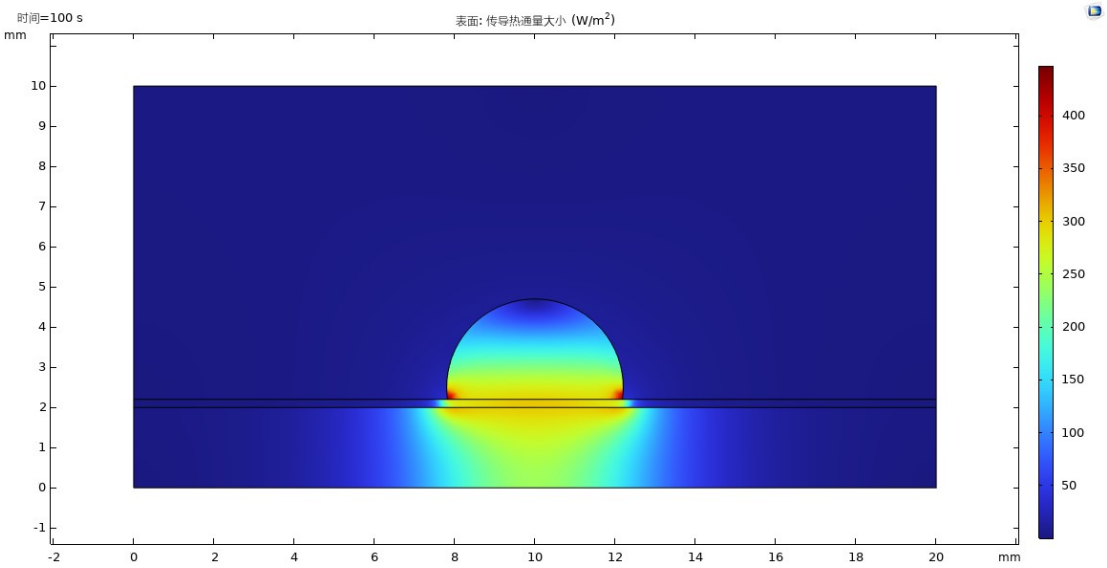

Fig. S15 The thermal conductivity behavior of PDMS surface simulated by COMSOL.

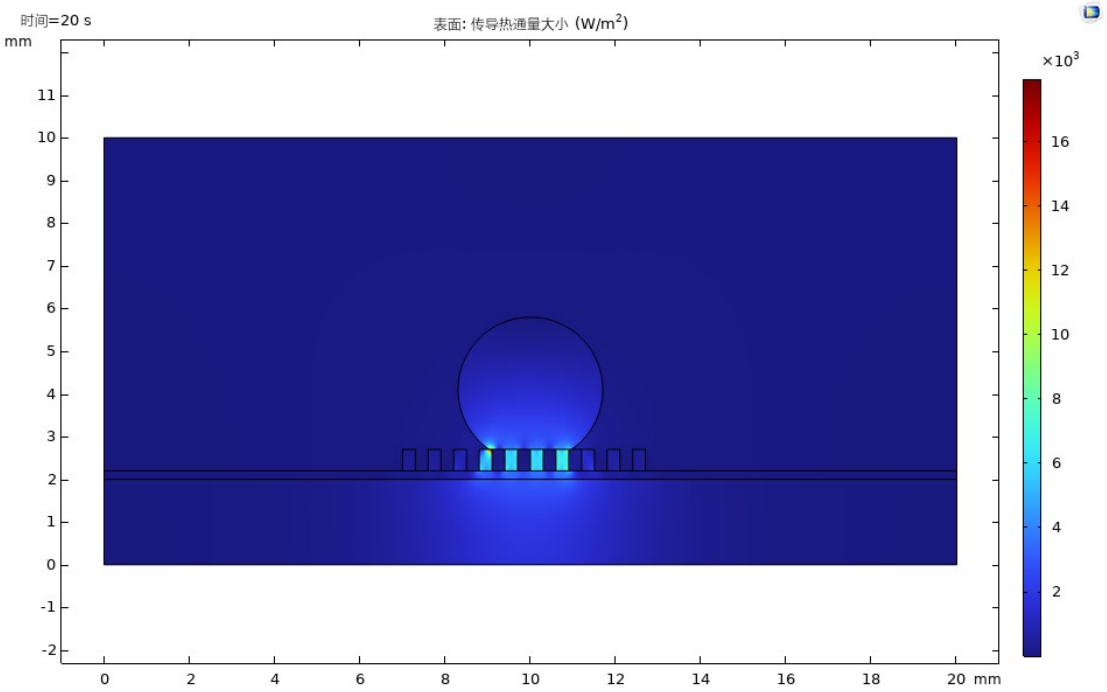

Fig. S16 The thermal conductivity behavior of BC surface simulated by COMSOL.

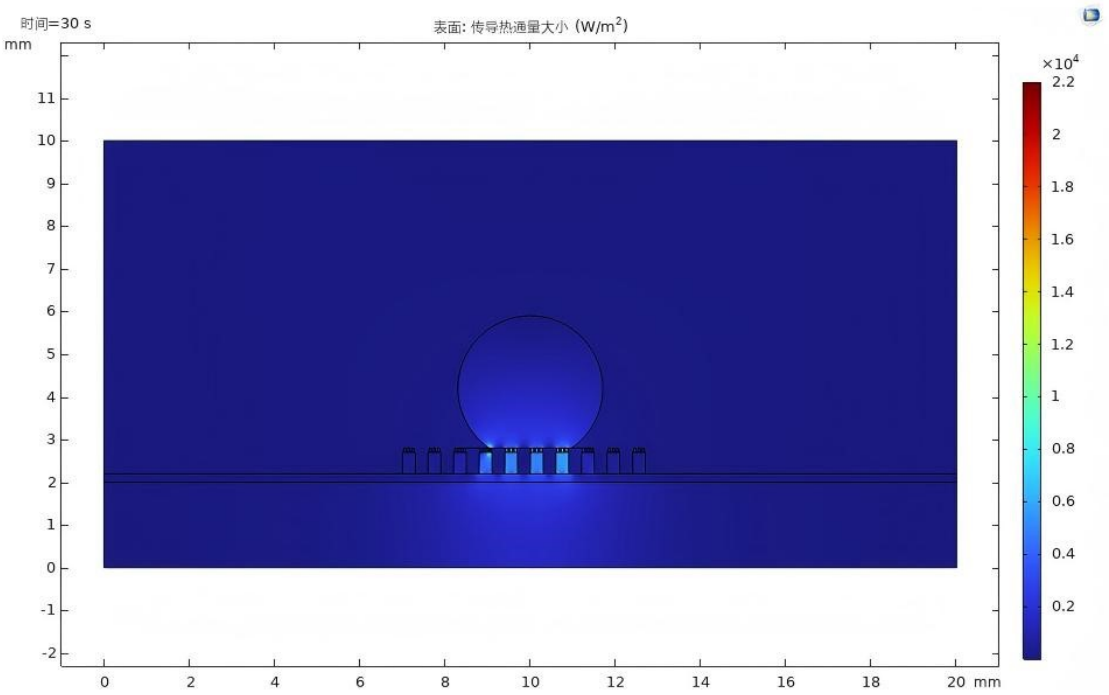

Fig. S17 The thermal conductivity behavior of Candle@BC surface simulated by COMSOL.

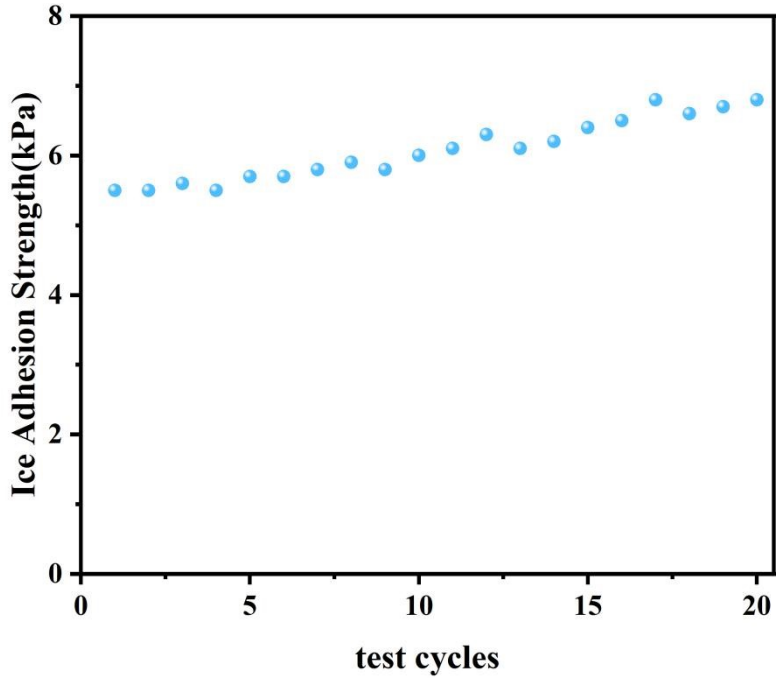

Fig. S18 Cyclic test of ice adhesion on the surface of Candle@BC.

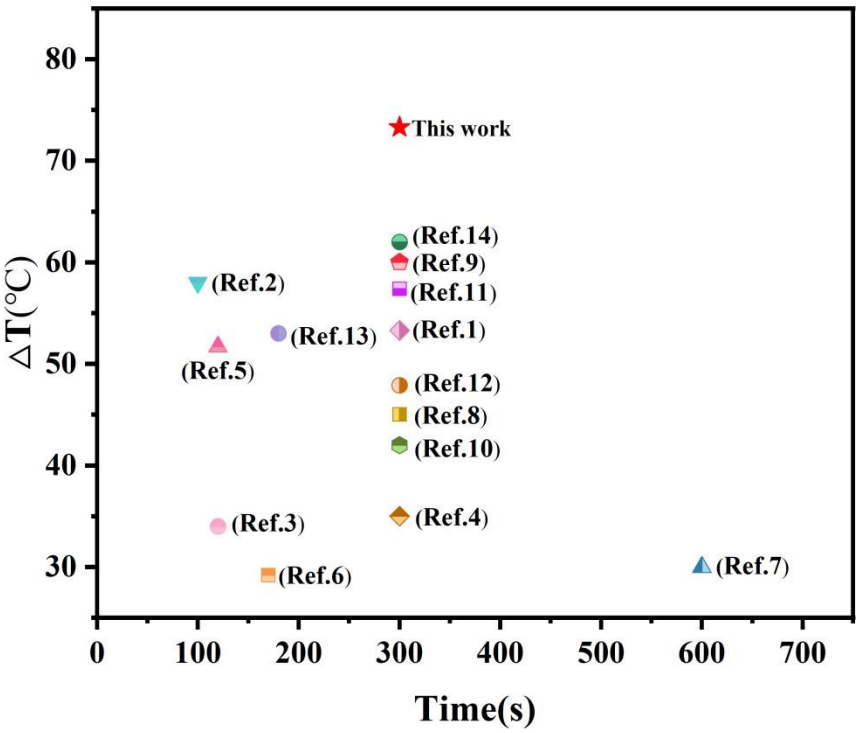

Fig. S19 comparison of photothermal performance of Candle@BC with other reported works.

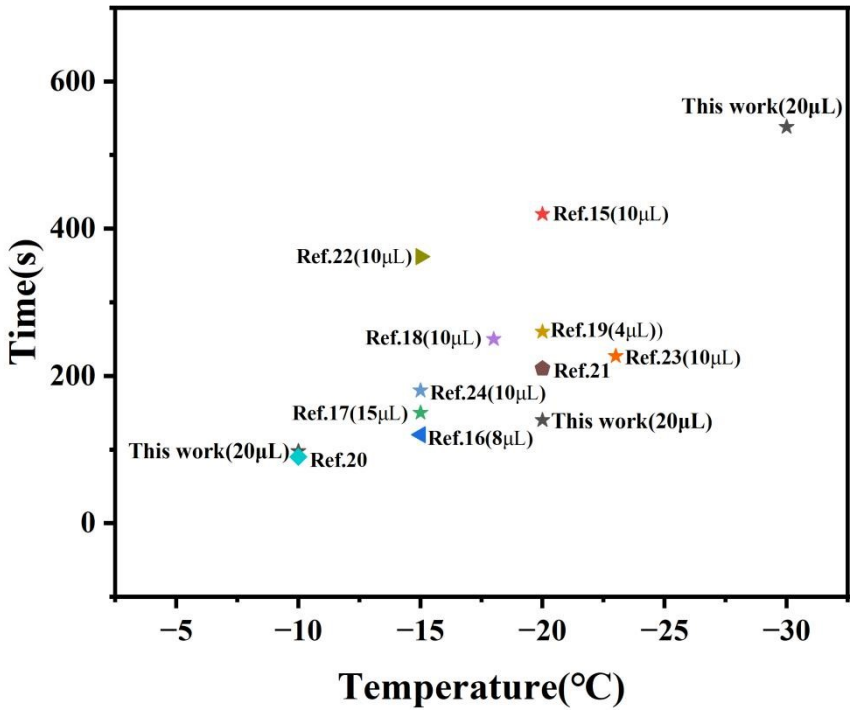

Fig. S20 comparison of photothermal de-icing performance of Candle@BC with other reported works.

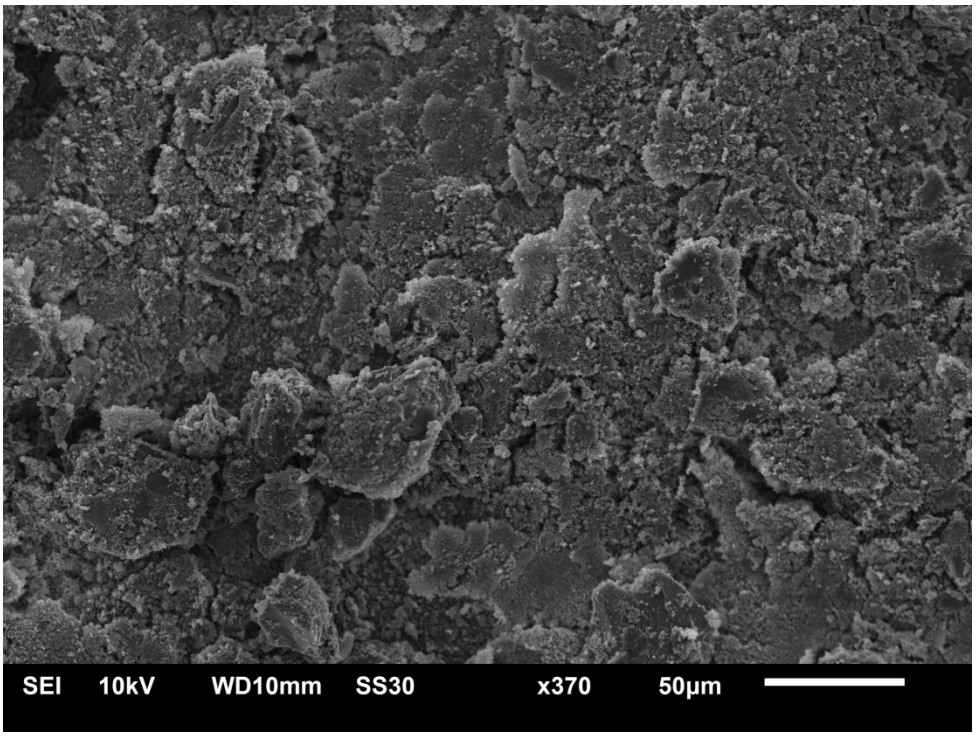

Fig. S21 SEM images of the Candle@BC surface after 50 cycles of sandpaper abrasion(370x).

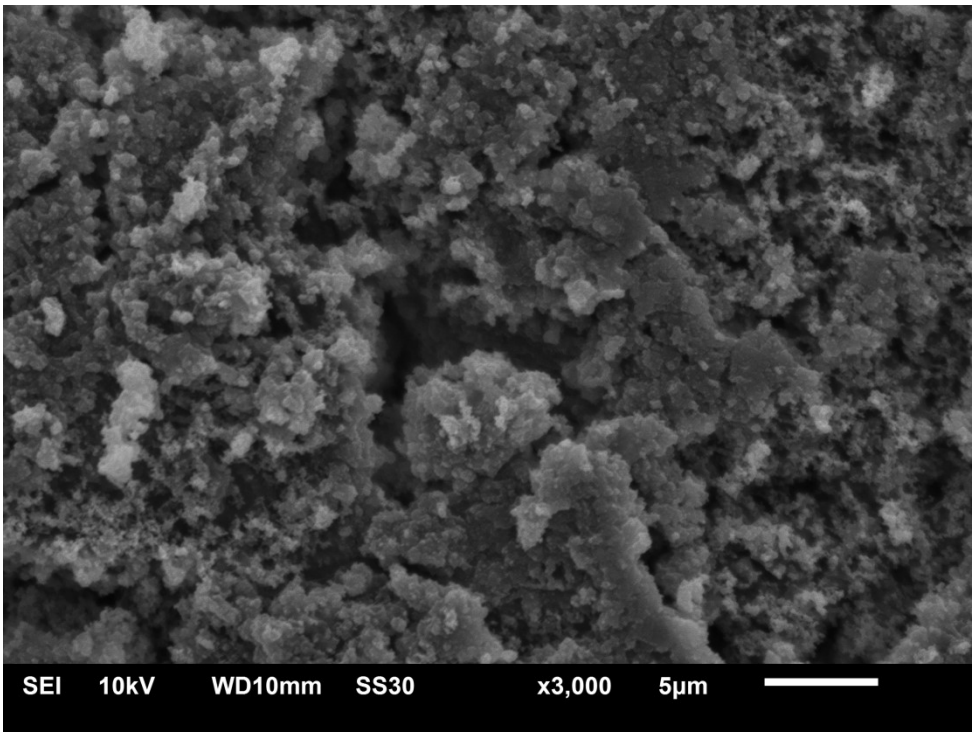

Fig. S22 SEM images of the Candle@BC surface after 50 cycles of sandpaper abrasion(3000x).

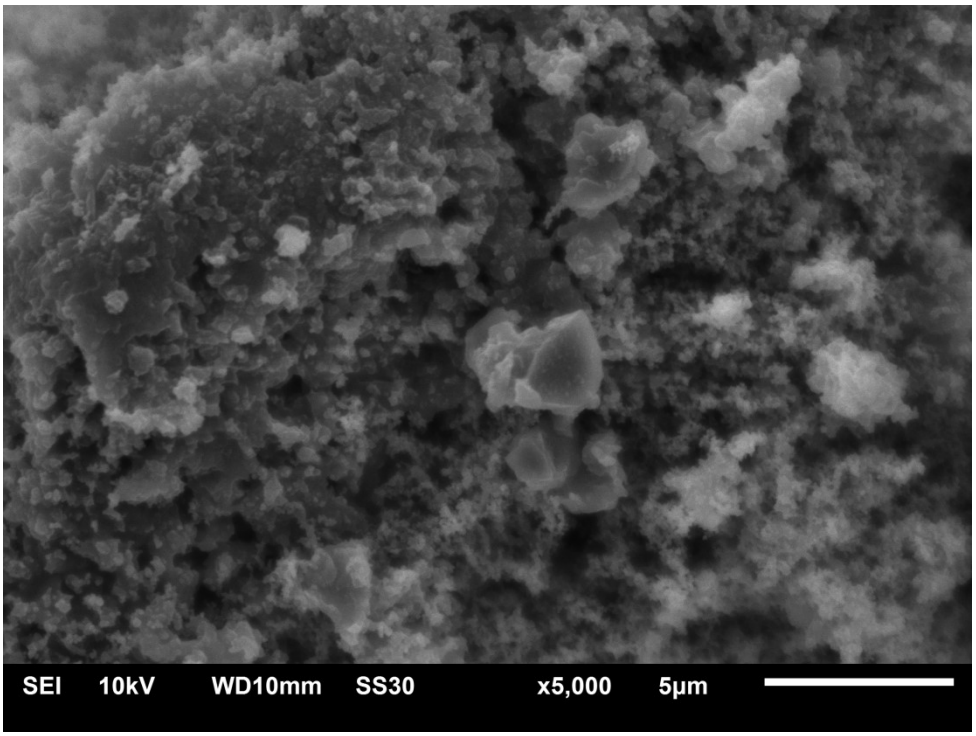

Fig. S23 SEM images of the Candle@BC surface after 50 cycles of sandpaper abrasion(5000x).

Reference

[1] Wu, S. W., Du, Y. J., Alsaida, Y., Wu, D., Hua, M. H., Yan, Y. C., Yao, B. W., Ma, Y. F., Zhu, X. Y., and He, X. M. Superhydrophobic photothermal icephobic surfaces based on candle soot. Proc. Natl. Acad. Sci. U. S. A., 2020, 117, 11240-11246. DOI: 10.1073/pnas.2001972117.

[2] Zhang, F., Xu, D., Zhang, D. W., Ma, L. W., Wang, J. K., Huang, Y., Chen, M. D., Qian, H. C., and Li, X. G. A durable and photothermal superhydrophobic coating with entwined CNTs-SiO_2 hybrids for anti-icing applications. Chem. Eng. J., 2021, 423, 130238. DOI: 10.1016/j.cej.2021.130238.

[3] Cai, C. Y., Wei, Z. C., Huang, Y. Z., and Fu, Y. Wood-inspired superelastic MXene aerogels with superior photothermal conversion and durable superhydrophobicity for clean-up of super-viscous crude oil. Chem. Eng. J., **2021**, 421, 127772. DOI: 10.1016/j.cej.2020.127772.

[4] Liu, Y. Wu, Y. Liu, R. Xu, S. Liu and F. Zhou, A Robust Photothermal Coating Strategy for Efficient Ice Removal, ACS Appl. Mater. Interfaces, 2020, 12, 51345–51376. DOI: 10.1021/acsami.0c13367.

[5] J. Zhang, X. Wang, L. Li, Y. Chen and H. Liu, Surface engineering of photothermal materials for anti-icing applications, Appl. Surf. Sci., 2023, 614, 157178. DOI: 10.1016/j.apsusc.2023.157178.

[6] M. Li, Z. Zhao, T. Wang, J. Li and Y. Ding, Multifunctional coatings with photothermal and icephobic properties, Adv. Mater., 2024, 36, 2410941. DOI: 10.1002/adma.202410941.

[7] X. Chen, R. Zhang, Y. Zhao and L. Jiang, Mechanical durability of photothermal anti-icing coatings, Int. J. Mech. Sci., 2024, 267, 109341. DOI: 10.1016/j.ijmecsci.2024.109341.

[8] Y. Wang, S. Liu, F. Zhou and J. Wang, Self-healing photothermal coatings for efficient

deicing, Chem. Eng. J., 2022, 450, 137936. DOI: 10.1016/j.cej.2022.137936.
[9] T. Wu, J. Li, X. Zhang and Y. Liu, Soft matter design for solar-driven anti-icing systems, Soft Matter, 2024, 20, 818a. DOI: 10.1039/d4sm00818a.
[10] H. Zhang, Y. Li, M. Xu and J. Zhang, Photothermal nanocomposites for extreme-environment deicing, Chem. Eng. J., 2024, 482, 158358. DOI: 10.1016/j.cej.2024.158358.
[11] L. Zhao, X. Wang, Y. Zhang and R. Chen, Thermal management in photothermal anti-icing materials, J. Mater. Sci. Technol., 2024, in press. DOI: 10.1016/j.jmst.2024.11.016.
[12] X. Li, Y. Zhou, J. Wu and L. Feng, Carbon-based photothermal coatings for anti-icing, Chem. Eng. J., 2021, 420, 132585. DOI: 10.1016/j.cej.2021.132585.
[13] Y. Zhang, H. Liu, M. Chen and Z. Wang, Recent advances in photothermal deicing materials, Chem. Eng. J., 2023, 451, 147553. DOI: 10.1016/j.cej.2023.147553.
[14] J. Wang, X. Li, Y. Zhao and T. Liu, Hierarchical photothermal surfaces for anti-icing and deicing, Chem. Eng. J., 2022, 450, 137461. DOI: 10.1016/j.cej.2022.137461.
[15] Y. Li, W. Ma, Y. S. Kwon, W. Li, S. Yao and B. Huang, Adv. Funct. Mater., 2022, 32, 2113297. DOI: 10.1002/adfm.202113297.
[16] Y. Ren, M. Hou, Z. Jiang, W. Sun, F. Chu and N. C. Lai, Surf. Coat. Technol., 2024, 485, 130888. DOI: 10.1016/j.surfcoat.2024.130888.
[17] B. Wu, X. Cui, H. Jiang, N. Wu, C. Peng, Z. Hu and D. Li, J. Colloid Interface Sci., 2021, 590, 301–310. DOI: 10.1016/j.jcis.2021.03.098.
[18] M. Zheng, C. Zhou, Q. Liu, X. Li, Y. Yang, Y. Sun and Q. Zhou, Soft Matter, 2023, 19, 9036–9049. DOI: 10.1039/d3sm00874a.
[19] M. Zhou, L. Zhang, L. Zhong, M. Chen, L. Zhu, T. Zhang and Y. Zheng, Adv. Mater., 2024, 36, 2310312. DOI: 10.1002/adma.202310312.
[20] X. Wei, F. Cai and J. Wang, Prog. Org. Coat., 2023, 182, 107696. DOI: 10.1016/j.porgcoat.2023.107696.
[21] J. J. Liu, C. Y. He, B. H. Liu, Z. Q. Wang, S. J. Zhao, Z. W. Lu and X. Aday, Chem. Eng. J., 2024, 489, 151338. DOI: 10.1016/j.cej.2024.151338.
[22] M. Hou, Z. Jiang, W. Sun, Z. Chen, F. Chu and N. C. Lai, Adv. Mater., 2024, 36, 2310312. DOI: 10.1002/adma.202310312.
[23] B. Wang, P. Yu, Q. Yang, Z. Jing, W. Wang, P. Li and Z. M. Wang, Mater. Today Phys., 2022, 24, 100683. DOI: 10.1016/j.mtphys.2022.100683.
[24] S. Zhang, F. Zhang, Z. Zhang, G. Li, H. Fu, J. Huang and Y. Lai, Chem. Eng. J., 2022, 450, 138328. DOI: 10.1016/j.cej.2022.138328.